Journal of Alloys and Compounds 882 (2021) 160608

Contents lists available at ScienceDirect

Journal of Alloys and Compounds

journal homepage: www.elsevier.com/locate/jalcom

$SrAl_2O_4$: Eu^{2+}, Dy^{3+} persistent luminescent materials functionalized with the Eu^{3+}(TTA)-complex by microwave-assisted method

Leonardo H.C. Francisco[a], Renan P. Moreira[a], Maria C.F.C. Felinto[a,*], Veronica C. Teixeira[b], Hermi F. Brito[c,*], Oscar L. Malta[d]

[a] Chemistry and Environment Center, Nuclear and Energy Research Institute (IPEN-CNEN), São Paulo, SP, Brazil
[b] Brazilian Synchrotron Light Laboratory, Brazilian Center for Research in Energy and Materials (LNLS-CNPEM), Campinas, Brazil
[c] Institute of Chemistry, University of São Paulo (IQ-USP), São Paulo, SP, Brazil
[d] Department of Fundamental Chemistry, Federal University of Pernambuco (dQF-UFPE), Recife, PE, Brazil

ARTICLE INFO

Article history:
Received 25 February 2021
Received in revised form 25 May 2021
Accepted 27 May 2021
Available online 3 June 2021

Keywords:
Strontium aluminate
β-diketonate
Persistent luminescence
Rare-earth

ABSTRACT

Recently, several classes of rare-earth-doped luminescent materials have been drawing attention due to structurally engineered energy converting systems, capable of tuning absorption and emission spectral ranges, outlining new materials and applications in photonics. In this scenario, this work presents the development of $SrAl_2O_4$:Eu^{2+},Dy^{3+} phosphors prepared by the *Pechini* method, which were further APTMS-functionalized (3-aminopropyltrimethoxysilane) by microwave-assisted synthesis, incorporating a Eu^{3+} β-diketonate complex embedded within a SiO_2-R network to increase light absorption and promote energy transfer processes. Powder X-ray diffraction data revealed a stable characteristic monoclinic phase of the $SrAl_2O_4$ host matrix, which undergoes structural changes after functionalization. Particle morphology and elemental distribution were probed by scanning electron microscopy technique, exhibiting surface alteration effects. Photoluminescence spectra displayed a characteristic broad green emission band assigned to the $4f^65d^1(^2D) \rightarrow 4f^7(^8S_{7/2})$ interconfigurational transition of the Eu^{2+} ion. Functionalized materials presented absorption shifts coupled with an emission band intensification suggesting effective interactions between the β-diketonate complex, the SiO_2-R network, and the inorganic host matrix. Increased absorption range and persistence decay time under near band gap excitation on modified materials were also observed.

1. Introduction

An ever-increasing development of research in fields like chemistry, photonics, and materials science has been promoting a growing interest in rare-earth doped materials for numerous applications, ranging from energy-converting materials for solar cells concentrators and lightning devices like LEDs (Light-emitting diode) and OLEDs (Organic light-emitting diode) to upconversion and persistent luminescent markers for temperature sensing and molecular probes towards theranostics and biomedicine [1–6].

Usually, the Eu^{3+} ion is used as a luminescent probe due to its well-separated narrow emission bands (~12,000 cm^{-1}) assigned to the $^5D_0 \rightarrow {}^7F_{0-6}$ transitions with non-degenerate ground state ($^7F_0$) and first emitting level ($^5D_0$) further facilitating spectral interpretation [7–9]. β-diketonate ligands are known for efficient absorption and energy transfer to the Eu^{3+} ion. Generally, RE^{3+} complexes are in hydrated form, *e.g.* $[Eu(tta)_3(H_2O)_2]$ (tta: thenoyltrifluoroacetone), which present high-energy oscillators (*i.e.*, vibronic O–H), leading to a high nonradiative contribution. Therefore, substituting water molecules with ancillary ligands (amide, phosphine oxide, pyridine N-oxide) in RE^{3+} complexes often improves their luminescence efficiency [10–15].

The most studied persistent luminescent materials are rare-earth doped aluminates and silicates-based phosphors (*e.g.*, $SrAl_2O_4$:Eu^{2+},Dy^{3+}; $Sr_4Al_{14}O_{25}$:Eu^{2+},Dy^{3+}; Ca_2MgSiO_7:Eu^{2+},Dy^{3+}, and $Ba_4(Si_3O_8)_2$:Eu^{2+},Dy^{3+}). Briefly, persistent luminescence is defined as a behavior where light emission continues for a period from seconds to days after excitation, which can be sunlight, visible light, UV radiation, X-rays, γ-rays, and electron beam. The persistent luminescence features are derived from trapping and thermal-stimulated recombination of charge carriers within the electronic structure of an inorganic matrix, being highly dependent on the trap nature (depth, concentration and energy level structure), which can be

* Corresponding authors.
E-mail addresses: mfelinto@ipen.br (M.C.F.C. Felinto), hefbrito@iq.usp.br (H.F. Brito).

https://doi.org/10.1016/j.jallcom.2021.160608
0925-8388/

intrinsic (structural defects, band gap) or imposed to the material (dopant and co-dopants ions, RE or transition metals, etc) [16–18].

The $SrAl_2O_4:Eu^{2+},Dy^{3+}$ phosphor is remarkable for its characteristic green emission and long decay time. This compound is based on the $(SrO)_n(Al_2O_3)_m$ mixed oxide system and has a stuffed tridymite structure composed of corner-sharing "rings" of AlO_4^- tetrahedra and Sr^{2+} ions distributed inside them. In this structure, Sr^{2+} occupies two slightly different crystallographic sites with the same coordination number (CN = 7) and similar average Sr–O bond lengths [19]. It is highlighted that ionic radii values imply that dopant substitution occurs at Sr^{2+} sites, and intrinsic defects of the monoclinic $SrAl_2O_4$ host matrix (such as oxygen vacancies, $V_O^{\bullet\bullet}$) [20,21] are responsible for trapping charge carriers (*e.g.,* electrons, e^-), leading to persistent luminescence phenomenon, even in the absence of co-dopant Dy^{3+} ions [22]. Thus, the role of Dy^{3+} in enhancing persistent luminescence arises from additional electron trapping, increasing energy storage compared to the capacity of $V_O^{\bullet\bullet}$ trapping alone. Furthermore, neighboring $V_O^{\bullet\bullet}$ and Dy^{3+} ions may also introduce pathways for thermal excitation of electrons in deeper traps to the conduction band [22], as electron transfer processes originating the from the Eu^{2+}-Dy^{3+} state to the metastable Eu^{3+}-Dy^{2+} state are also known to take place in the strontium aluminate luminescent materials as reported in reference [23].

Moreover, in spite of the similarity of both Sr^{2+} sites, two distinct Eu^{2+} emission bands, typically around 450 nm (blue) and 520 nm (green) are commonly observed at low temperature measurements reported in the literature, though is known that blue Eu^{2+} emission is completed quenched at 300 K. Mainly, these spectral features are the consequence of the small but significant difference between the two Sr^{2+} lattice sites in monoclinic $SrAl_2O_4$, as reported by Botterman et al. [24].

Essentially, high green emission of $SrAl_2O_4:Eu^{2+},Dy^{3+}$ is assigned to the $4f^65d^1(^2D)\rightarrow 4f^7(^8S_{7/2})$ transitions of Eu^{2+} ion, where the co-dopant Dy^{3+} energy levels that act as electrons traps are located near the bottom of the conduction band (CB) of the $SrAl_2O_4$ matrix. Usually, the Eu^{2+} ion shows a broad emission that is strongly affected by the chemical environment and may undergo severe blue or red-shifts due to the crystal field effect. Thus, $SrAl_2O_4:Eu^{2+},Dy^{3+}$ excitation commonly takes place at UV-range corresponding to a high-intensity Eu^{2+} absorption band. Besides, near band gap excitation can also be used to promote green luminescence, as (Eu^{2+}) $4f^65d^1$ excited states partially overlap with the bottom of CB in this matrix [25–27].

Thus, this work proposes the incorporation of the europium complex $[Eu(tta)_3(4\text{-picNO})_2]$ (4-picNO: 4-picoline N-oxide) on the surface of $SrAl_2O_4:Eu^{2+},Dy^{3+}$ phosphor by SiO_2-R linkage, supporting the host matrix and complex functionalization. This approach aims to enhance characteristic green light emission from Eu^{2+} activator doped into $SrAl_2O_4$ host matrix due to potential increased energy absorption as well as energy transfer processes.

2. Experimental

2.1. Materials

All materials used in the synthesis were purchased from Sigma-Aldrich, Synth, and VETEC and used without further purification. The purity of the employed reagents follows Europium Oxide (Eu_2O_3, 99.9%), Dysprosium Oxide (Dy_2O_3, 99.9%), Strontium Nitrate ($Sr(NO_3)_2$, 99%), Aluminium Nitrate Nonahydrate ($Al(NO_3)_3.9(H_2O)$, 99%), 2-Thenoyltrifuoracetone (tta: $C_8H_5F_3O_2S$, 99%), 4-picoline N-oxide (4-picNO: C_6H_7NO, 98%), 3-Aminopropyltrimethoxysilane (APTMS: $H_2N(CH_2)_3Si(OCH_3)_3$, 97%), Nitric Acid (HNO_3, 65%), Hydrochloric Acid (HCl, 37%), Citric Acid ($C_6H_8O_7$, 99%), Ethylene Glycol ($C_2H_6O_2$, 99%), Ammonium Hydroxide (NH_4OH, 30%), Ethyl Alcohol (C_2H_5OH, 99.5%), Acetone (C_3H_6O, 99.5%) and Granular Activated Charcoal (99%).

2.2. Synthesis of rare-earth precursors

Starting from the rare-earth metal oxides (RE_2O_3, RE: Eu^{3+} or Dy^{3+}), the preparation of $RE(NO_3)_3.6H_2O$ and $EuCl_3.6H_2O$ was carried out by suspending the metal oxides in distilled water and stirring the mixtures at low heating (80 °C) as a dropwise addition of nitric acid or hydrochloric acid were added for the synthesis of metal nitrates and europium chloride respectively. These compounds were crystallized with solvent evaporation and further dried at room temperature under reduced pressure in a vacuum desiccator.

2.3. Preparation of $SrAl_2O_4:Eu^{2+},Dy^{3+}$ phosphors

$Sr_{0.94}Al_2O_4:Eu^{2+}_{0.02},Dy^{3+}_{0.04}$ phosphor was prepared *via* the Pechini method [28], where strontium aluminate matrix was doped with 0.02 and 0.04 molar of europium and dysprosium, respectively. In this procedure, a stoichiometric amount of metal nitrates $M(NO_3)_x{\cdot}n(H_2O)$; (M: Sr^{2+}, Al^{3+}, Eu^{3+}, and Dy^{3+}) aqueous solutions were mixed together and stirred at room temperature. An aqueous solution of citric acid (3:1 molar ratio to metal ions) was slowly added to the nitrate solution, resulting in metal-citrate complexes. Shortly after, a set volume (50 mL) of ethylene glycol was further added to this solution, which was kept under constant stirring (at roughly 300 rpm) until the formation of a characteristic transparent viscous gel which was dried at 300 °C for 6 h, yielding a polymeric precursor of strontium aluminate. This precursor was pulverized to obtain a fine powder that was further annealed at 1100 °C for 6 h with granular activated charcoal on a high-temperature resistance oven, promoting $Eu^{3+}\rightarrow Eu^{2+}$ reduction due to carbon monoxide producing the $SrAl_2O_4:Eu^{2+},Dy^{3+}$ (SAO) phosphor.

2.4. Synthesis of Europium β-diketonate complexes

For the synthesis of a hydrated europium complex $[Eu(tta)_3(H_2O)_2]$, the dissolution of 2-thenoyltrifluoroacetone ligand was carried out in ethanol (60 mL) at low heating (50 °C), followed by a dropwise addition of ammonium hydroxide until pH 7. This solution was kept under constant stirring with the addition of a stoichiometric amount of $EuCl_3.6H_2O$ aqueous solution. Ammonium hydroxide was further employed until pH 7 was reached. The mixture was kept under constant stirring for 2 h, yielding a characteristic yellowish oil, followed by pale yellow powder precipitation of $[Eu(tta)_3{\cdot}n(H_2O)]$. This crystalline solid product was filtered and dried at room temperature. Powder recrystallization was carried out in ethanol solution, where the $[Eu(tta)_3(H_2O)_2]$ complex was successfully obtained. For the coordination of the 4-picNO ancillary ligand into the europium complex, the previously prepared $[Eu(tta)_3(H_2O)_2]$ complex was dissolved in acetone under continuous stirring at 50 °C, and the stoichiometric volume of a 4-picNO acetone solution was added to the mixture. After solvent evaporation and further recrystallization in acetone, the $[Eu(tta)_3(4\text{-picNO})_2]$ complex was obtained. The crystalline solid was dried at room temperature under reduced pressure in a vacuum desiccator.

2.5. Microwave-assisted surface functionalization

For the surface functionalization of the previously prepared phosphor, a set amount (2% molar ratio to $SrAl_2O_4:Eu^{2+},Dy^{3+}$) of the $[Eu(tta)_3(4\text{-picNO})_2]$ complex was suspended in APTMS aqueous solution and kept under stirring at room temperature for 0.5 h. $SrAl_2O_4:Eu^{2+},Dy^{3+}$ was further added to the mixture, which was submitted to ultrasound and microwave cycles (5 min at 25 °C and 1 min at 900 W, respectively). This step was repeated five times until

a viscous solution was obtained, which was set at 25 °C (room temperature) for 24 h. This mixture was further dried at 150 °C and exceeding APTMS was removed through centrifugation with distilled water at 3000 rpm, yielding a $SrAl_2O_4:Eu^{2+},Dy^{3+}@(SiO_2\text{-}R)\text{-}[Eu(tta)_3(4\text{-}picNO)_2]$ compound (SAO@SE). Moreover, a $SrAl_2O_4:Eu^{2+},Dy^{3+}@(SiO_2\text{-}R)$ sample (SAO@S) was also prepared by skipping the addition of the $[Eu(tta)_3(4\text{-}picNO)_2]$ complex at the beginning of the synthesis procedure. Both samples were dried and kept at room temperature under reduced pressure in a vacuum desiccator.

2.6. Instrumental

Infrared transmittance analysis was performed by Fourier Transform Infrared Spectroscopy (FTIR) measurements on a Shimadzu IR-Prestige 21 spectrophotometer with a 1 cm^{-1} point resolution within the 4000–500 cm^{-1} energy range using a KBr carrier with 1% w.t. sample concentration. X-ray diffraction patterns were obtained by $K\alpha_{Cu}$ radiation on a Rigaku Miniflex II diffractometer within 3–80° (2θ) range, using a 0.03° s^{-1} step width under 30 kV voltage and 15 mA current. Scanning Electron Microscopy (SEM) images were acquired on a HITACHI TM3000 microscope at 15 kV voltage *via* Backscattered Electrons (BSE), while Energy Dispersive Spectroscopy (EDS) data was obtained through an XFlash 430H detector for the 0.4–10 keV energy range and processed by Quantax70 software in the same equipment. Transmission electron microscopy (TEM) images were acquired on a JEOL JEM 2100 microscope with a LaB_6 filament under 200 kV voltage.

Several spectroscopy techniques were applied to investigate the luminescent properties and electronic structure of the prepared materials. Diffuse Reflectance Spectroscopy (DRS) data was obtained through a Shimadzu UV-2600 spectrophotometer by an integrating sphere in the 220–1400 nm spectral range with a 0.1 nm s^{-1} step width, using $BaSO_4$ as a standard reference. Emission and excitation luminescence spectra were recorded on a HORIBA Fluorog-3 spectrofluorometer with a Xenon lamp of 450 W as excitation source and processed by FluorEssence software. Emission spectra were acquired on an axial setup of 22.5° with a blazed holographic grating of 1200 lines/mm and recorded by a Charge-Coupled Device (CCD) detector while excitation measurements were registered by a photomultiplier (PMT) with a 1 nm s^{-1} step width.

Finally, synchrotron radiation measurements were performed at the Brazilian Synchrotron Light Laboratory (LNLS) on the Toroidal Grating Monochromator (TGM) beamline, which is dedicated to Vacuum-UV (VUV) spectroscopy techniques in the 3–300 eV energy range. Total photoluminescence (excitation) measurements [29] were acquired by a PMT (R928, Hamamatsu) detector with 0.1 eV point resolution within 4.5–7.5 eV range, while a CCD detector (QE 65000, Ocean Optics) recorded emission (3D) spectra for the 400–800 nm range. Persistent luminescence decay curves were recorded by PMT for samples excited by 6.7 and 6.9 eV photons immediately after terminating excitation. All measurements were performed at room temperature (300 K) and pressure better than 10^{-7} mbar using a 200 nm thick quartz slide to avoid second-order harmonics from the beamline optics while the acquired signal was collected by an optical fiber (SR UV-Vis, aperture 600 µm, Ocean Optics) and further corrected applying sodium salicylate (Synth) as a standard reference.

3. Results and discussion

3.1. Structural analysis

Firstly, the composition of the prepared materials was characterized by FTIR spectroscopy by probing principal vibrational modes associated with phase formation and coordination. In the transmittance spectra obtained for $SrAl_2O_4:Eu^{2+},Dy^{3+}$ (Fig. S1a, where all figures with "S" are presented in the Supplementary Information), several stretching modes of υAl–O and υSr–O–Al were identified, alongside with υSr–O. The multiple peaks within this spectral region are assigned to distinct vibrational modes of four non-equivalent AlO_4^- tetrahedra. Furthermore, a weak υO–H stretching mode indicates low water content adsorbed on the particle surface of the $SrAl_2O_4$ host-matrix [30].

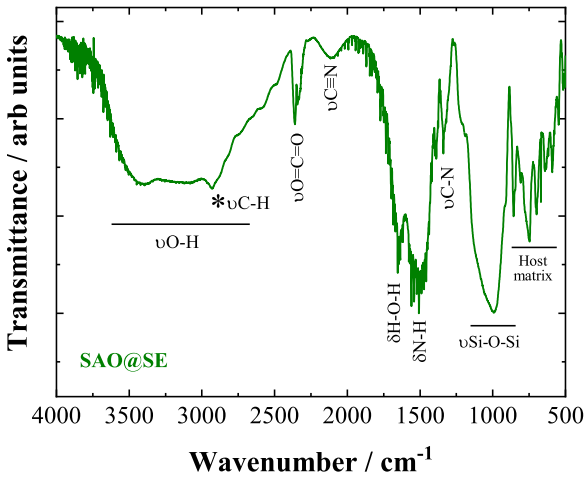

Fig. 1. FTIR transmittance spectra of the functionalized SAO@SE ($SrAl_2O_4:Eu^{2+},Dy^{3+}@SiO_2\text{-}[Eu(tta)_3(4\text{-}picNO)_2]$) material.

In contrast, transmittance spectra for the SAO@S (Fig. S1b) and SAO@SE (Fig. 1) materials presented a different profile, highlighting vibrational modes derived from the SiO_2-R network. A strong υSi–O–Si is observed around 1000 cm^{-1}, alongside a υC-H component overlapping with the intense υO–H stretching. Together, the υO-H and δH–O–H vibrational modes also imply significant water adsorption throughout the surface of the functionalized materials. Host matrix phase changes – which will be addressed further – derived from microwave-assisted synthesis also modify the relative intensity of the spectral profile within the 1000–500 cm^{-1} range. Finally, the intense δN-H band uncovers the presence of the amino group ($-NH_2$) within the SiO_2-R network, as the absence of characteristic υSi–O–C stretching derived from APTMS precursor implies in the formation of a polymeric silica network [31].

For the europium β-diketonate complexes, strong convolution and high infrared absorption bands at lower energies turn individual attribution of distinguished vibrational modes a challenge (Fig S2a and S2b). In general, the infrared spectra profile of the hydrated $[Eu(tta)_3(H_2O)_2]$ complex has a good agreement with spectroscopic data reported in the literature [32]. The substitution of water molecules by the 4-picNO ligand in the Eu^{3+} coordination polyhedron the $[Eu(tta)_3(4\text{-}picNO)_2]$ complex was indicated by vanishing of the υO-H band (~3600 cm^{-1}) of the water molecules as well as by the presence of υN-O. Characteristic vibrational modes of tta ligand are also observed, such as υC-F stretching attributed to ($-CF_3$) group (~1300 cm^{-1}) was also observed. It is noteworthy that a low concentration of the $[Eu(tta)_3(4\text{-}picNO)_2]$ complex on the $SrAl_2O_4$ matrix, the vibrational modes were not observed for the SAO@SE system.

The powder X-ray diffraction (PXRD) patterns recorded for all compounds (Fig. 2 a, b), show that after annealing the amorphous polymeric precursor, a good agreement of the diffraction pattern with the Inorganic Crystal Structure Database (ISCD) standard $SrAl_2O_4$ (160296) monoclinic phase [Space group: P 1 2_1 1 (4), Z = 4] was found for the SAO phosphor (Fig. 2a, blue line). The crystal structure for $SrAl_2O_4$ made on Diamond 4 software is in agreement with the stuffed-tridymite structure (Fig. 2c), and monoclinic unit cell (Fig. 2d) reported in the literature [33].

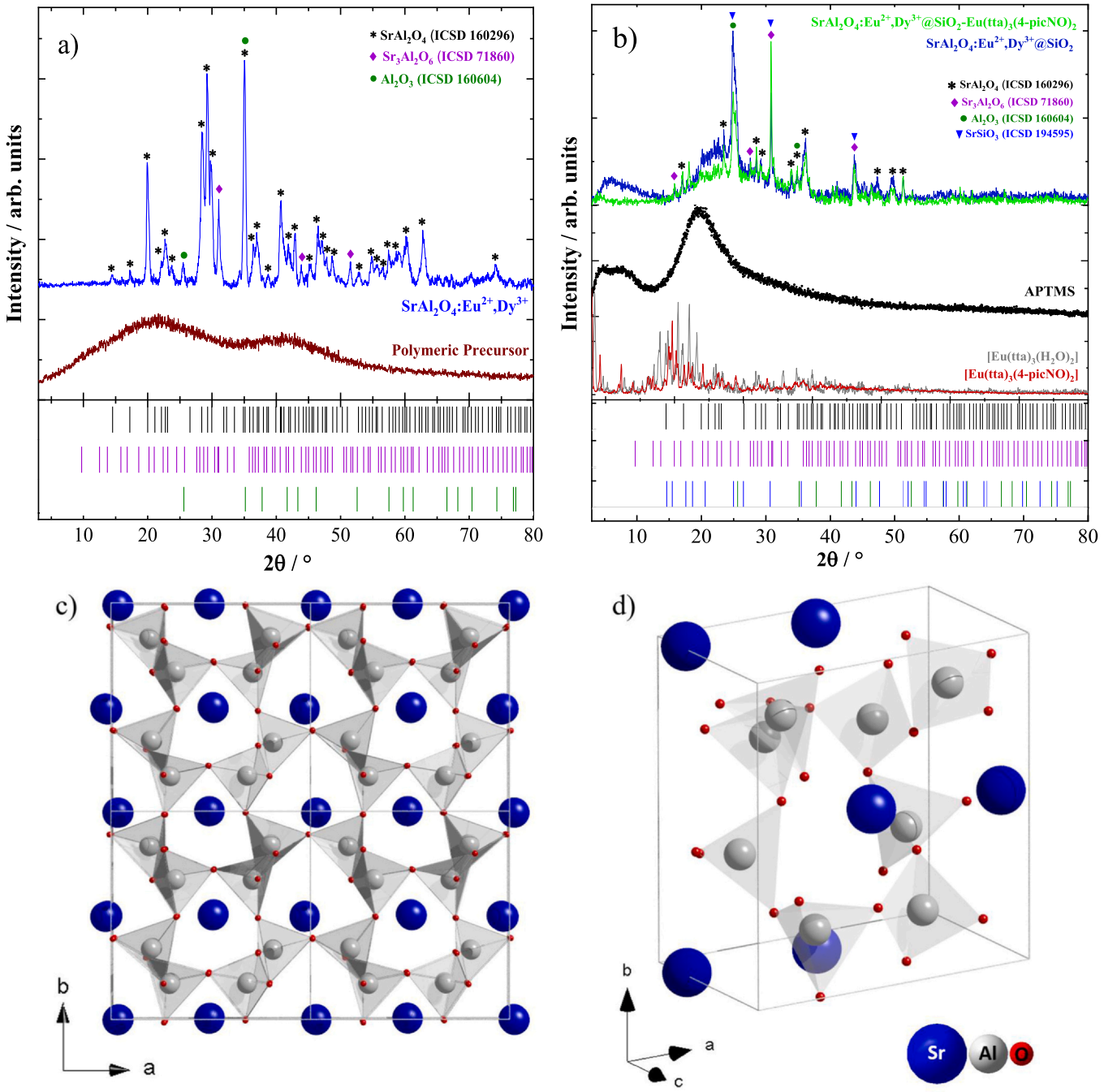

Fig. 2. PXRD profiles of (a) SAO ($SrAl_2O_4$:Eu^{2+},Dy^{3+}) phosphor and its polymeric precursor, (b) SAO@S ($SrAl_2O_4$:Eu^{2+},Dy^{3+}@SiO_2) and SAO@SE SE ($SrAl_2O_4$:Eu^{2+},Dy^{3+}@SiO_2-[Eu(tta)$_3$(4-picNO)$_2$]) functionalized materials alongside APTMS and [Eu(tta)$_3$(L)$_2$ (L: H_2O or 4-picNO)] complexes. Several standard ICSD patterns of correlated structures are presented. The stuffed tridymite structure (c) and unit cell (d) of the prepared $SrAl_2O_4$ host matrix built on Diamond 4 software is also shown.

A secondary phase derived from a different stoichiometry of $(SrO)_n(Al_2O_3)_m$ is observed alongside with α-Al_2O_3 formation compensating for the n/m ratio. The residual $Sr_3Al_2O_6$ by-product formation (3% estimated by reference intensity ratio) has a cubic crystal structure and highly distinct Sr^{2+} coordination polyhedron compared to the standard $SrAl_2O_4$ host matrix, which may imply in different spectroscopic behavior of europium ions embedded within the $Sr_3Al_2O_6$ structure. As for the α-Al_2O_3 by-product, Al^{3+} ions are commonly replaced by 3d group impurities, as substitution by RE^{3+} dopants is not favourable due to its larger ionic radius [34]. Also, the stoichiometric composition does not favor rare-earth oxide (Eu_2O_3 or Dy_2O_3) formation.

PXRD profiles of SAO@S and SAO@SE materials show structural changes, including the phase formation of $SrSiO_3$ together with a substantial contribution of amorphous SiO_2 phase, due to the APTMS functionalization. Also, it is observed that the diffraction peak relative intensities of the $SrAl_2O_4$ matrix greatly diminishes, while an overlapping high-intensity reflection of $SrSiO_3$, α-Al_2O_3, and $Sr_3Al_2O_6$ are observed. Therefore, a somewhat mixed structure of polycrystalline $SrAl_2O_4$, $Sr_3Al_2O_6$, $SrSiO_3$, α-Al_2O_3, and amorphous SiO_2 is predominant for the functionalized compounds. Europium complexes PXRD patterns data indicated that there are no significant contributions for the SAO@SE material.

Crystallite size for the SAO phosphor was determined by the Scherrer method [35], applying a NaCl pattern as a standard correction for the full width at half maximum (FWHM) parameter. As the FWHM parameter commonly varies widely throughout X-ray

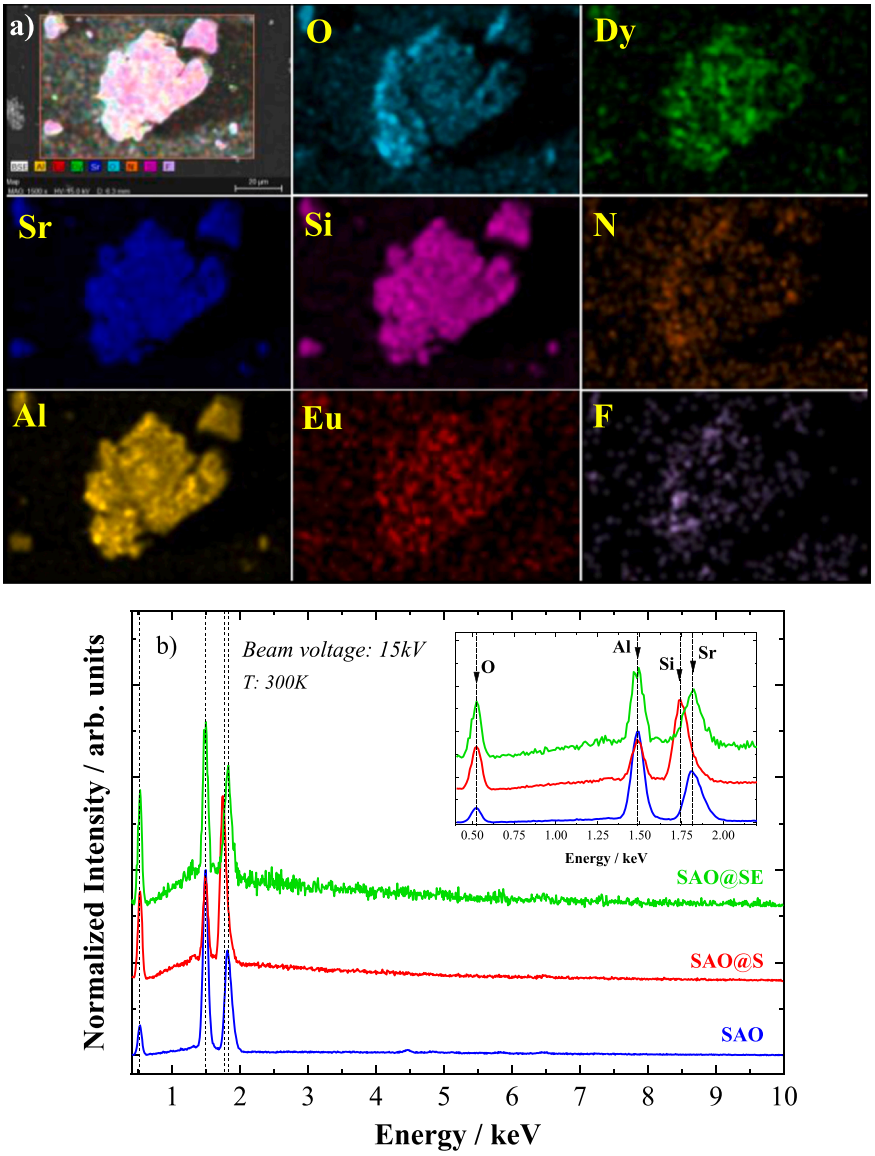

Fig. 3. (a) Elemental mapping for SAO@SE ($SrAl_2O_4:Eu^{2+},Dy^{3+}$@$SiO_2$-[$Eu(tta)_3(4\text{-picNO})_2$]) probing Sr, Al, O, Si, Eu, Dy, N, and F element distributions. (b) EDS emission spectra of strontium aluminate compounds under 15 kV electron beam showcasing Sr, Al, O and Si characteristic X-ray emission.

diffraction patterns, an approach of plotting crystallite size as a function of d_{hkl} was used to obtain a more precise estimate, yielding a medium size of roughly 26 nm (Fig. S3). The experimentally obtained d_{hkl} values used for the crystallite size calculations are listed in Table S3. On the other hand, crystallite size distributions for the SAO@S and SAO@SE samples were not included due to the low relative intensity of the collected signal alongside the broad SiO_2 band overlapping with a significant number of the observed diffraction peaks, which directly affects the FWHM parameter.

SEM images of all materials probed the morphology and surface alteration effects of functionalization by BSE contrast measurements. For the SAO material (Fig. S4a), well-defined surfaces are observed, indicating a high degree of crystallinity with particle size about 20–30 μm – for large particles – and about 5–10 μm for medium-sized particles. However, much smaller regions (≈1 μm) were also identified. Yet, the structural data were not collected at this magnitude due to instrumental and experimental conditions. It is noteworthy that the microparticles presented in SEM images are polycrystalline, such as indicated by the smaller crystallite size calculated from the PXRD data, as crystallite size corresponds to ordered diffraction domains, whereas microparticles are constituted of several aggregated crystallites. For the modified SAO@S (Fig. S4b) and SAO@SE (Fig. S4c) materials, a pronounced surface-related effect is noted, where a porous-like structure of the SiO_2-R network is verified. Still, no significant alteration of the morphological behavior was detected due to [$Eu(tta)_3(4\text{-picNO})_2$] complex incorporation.

Elemental distribution obtained by characteristic X-ray emission (EDS) revealed a homogeneous composition and dopant distribution for all materials (Fig. 3a and Fig. S4-S5), indicating the efficiency of the microwave-assisted synthesis as a route to integrate a SiO_2-R network at the surface of strontium aluminate phosphors. Furthermore, characteristic $K_{\alpha N}$ emission on functionalized compounds suggests the presence of amino groups (R-NH_2) from APTMS, while the distribution of [$Eu(tta)_3(4\text{-picNO})_2$] complex was probed by $K_{\alpha F}$ derived from the (CF_3) tta terminal group. X-ray emission spectra (Fig. 3b) outlined characteristic emission lines for Sr, Al, O, and Si, alongside *bremsstrahlung* radiation. A low energy spectral shift of the $K_{\alpha Si}$ SAO@S sample is likely due to exceeding APTMS compared to SAO@SE, which presents a broader $K_{\alpha Sr}$ emission regarding the non-modified SAO phosphor. The characteristic X-ray emission of the Eu and Dy dopants are not observed (typically L lines within 5–7 keV region) in EDS spectra, owing to the low doping concentration, still,

elemental distribution maps did capture Eu and Dy signal (Fig. 3a), which was found to be uniform in strontium aluminate particles.

TEM images of the SAO@SE material give information of the silica polymeric network on top of the SAO phosphor, where it was observed a SiO_2 coating as small as 10 nm (Fig. 4a). Crystalline phases were also identified in the SAO/SiO_2 interface (Fig. 4b) extending deep into the SiO_2 coating, with an interplanar spacing of 3.536 Å (Fig. S7) assigned to (1,0,0) planes derived from crystalline $SrSiO_3$ phase formation as previously indicated by PXRD. Several crystallites of a few nanometers width embedded in the amorphous SiO_2 background were also recognized (Fig. 4c).

3.2. Luminescent properties

The DRS spectra for strontium aluminate compounds (Fig. 5a) give information on absorption bands from the $SrAl_2O_4$ host matrix and characteristic intraconfigurational 4f transitions of the Eu and Dy dopants. Besides, DRS analysis was employed due to the mixed oxide wide band gap nature of the strontium aluminate host matrix [36]. A similar spectral profile is noted for all analyzed samples in the region from visible to near-infrared (NIR) (700–1400 nm), show absorption bands assigned to 4f–4f transitions of Dy^{3+} ion. However, a distinct behavior is noted for SAO@S (Fig. 5a blue line), and SAO@SE (Fig. 5a green line) functionalized samples compared to the SAO phosphor, where an intense absorption band of SiO_2 at 256 nm is observed. Moreover, for the SAO@SE compound, a significant contribution (broadening) is assigned to $S_0 \rightarrow S_n$ transitions derived from the $[Eu(tta)_3(4\text{-picNO})_2]$ complex. It is also noted that Eu^{2+} absorption bands also overlap with host-matrix, SiO_2 and ligand absorption bands. Still, in Fig. 5b, it is possible to verify 4f–4f absorption transitions of both Eu^{3+} and Dy^{3+} ions, being the first indication of the presence of non-reduced Eu^{3+}. These transitions are not observed for the SAO@SE sample due to strong spectral overlap with allowed $S_0 \rightarrow S_n$ transitions.

Band gap energy (E_g) was first estimated (Fig. S8) by the single-constant Kubelka-Munk function (Eq. (1)) *via* DRS [36–38].

$$[F(R_\infty)h\nu]^{1/n} = [(K/S)h\nu]^{1/n} \quad (1)$$

Where K and S represent the material's absorption and scattering coefficients, given by $(1 - R_\infty)$ and $2R_\infty$ respectively, while R_∞ corresponds to the experimentally measured reflectance, and n stands for the transition constant, assuming values of ½ or 2 for direct and indirect allowed transitions accordingly. Furthermore, h corresponds to Planck's constant and ν to the photon's frequency.

For the SAO phosphor, as no minimum R_∞ peak value was recorded within the studied spectral region, and a linear fit model was performed to estimate absorption in the higher-energy UV range, set as $(R_\infty \rightarrow 0)$. Furthermore, the linear regions of the Kubelka-Munk functions have been extrapolated to the energy axis intercept, finding E_g values derived from $[F(R_\infty)h\nu]^{1/n} \rightarrow 0$. These regions were set as the interval between linearity deviation by saturated transition states at high energy, and the characteristic *Urbach tail* at the lower energy end, referring to near band gap edge defects absorption states.

Thus, the SAO phosphor presented E_g = 6.62 and 6.53 eV for direct and indirect allowed transitions, respectively, corroborating with experimental band gap energy values previously reported in the literature for the $SrAl_2O_4$ host matrix [39]. However, band gap values estimated for SAO@S (E_g = 4.32 and 3.63 eV) and SAO@SE compounds (E_g = 4.30 and 3.54 eV) unveiled the introduction of new energy levels within the electronic structure of the host matrix by the functionalization process, as the intense ligand (tta and 4-picNO) and SiO_2 absorption in the near-UV region dominated the DRS spectra. The statistical parameters of the coefficient of determination (R^2) and residual sum of squares (RSS) presented suitable values for a high-precision linear fitting for extrapolation.

Luminescence spectroscopy was first performed for both europium β-diketonate complexes to investigate energy transfer processes and the ancillary ligand coordination. Excitation spectra monitored on the characteristic Eu^{3+} emission (λ_{em}: 612 nm) for the $[Eu(tta)_3(L)_2]$ complexes (L: H_2O or 4-picNO) are presented in Fig. S9a. Spectral profiles reveal strong ligand absorption assigned to the $S_0 \rightarrow S_n$ transitions and narrow bands attributed to $^7F_0 \rightarrow {}^5L_6$, $^7F_1 \rightarrow {}^5D_3$ and $^7F_0 \rightarrow {}^5D_2$ transitions of the Eu^{3+}. An increase of FWHM for ligand absorption bands in the $[Eu(tta)_3(4\text{-picNO})_2]$ complex may be assigned to overlapping tta and 4-picNO energy states.

Emission spectra under 394 nm excitation Fig. S9b shows intense red emission of the hypersensitive (Eu^{3+}) $^5D_0 \rightarrow {}^7F_2$ transition, indicating the "antenna effect" of ligand→Eu^{3+} energy transfer (ET) by the absence of ligand phosphorescence in the visible range. The coordinated ligand (4-picNO) alters the emission profile in a significant manner, leading to an overall increase of emission intensity. As the first emitting and ground states of the Eu^{3+} ion are non-degenerate (*e.g.* J = 0), the analysis of emission profiles grants valuable information on structure parameters of the Eu^{3+} point group. For the $[Eu(tta)_3(H_2O)_2]$ complex, the $^5D_0 \rightarrow {}^7F_0$ transition presents mainly one intense emission peak, alongside three main $^5D_0 \rightarrow {}^7F_1$ components (Fig. S9b, blue line), suggesting that most of the Eu^{3+} ion occupies a single site of symmetry, where some weak emission peaks observed for the $^5D_0 \rightarrow {}^7F_{0-1}$ transitions exceeding the maximum number of *Stark* levels (2J+1) may suggest the formation of a low content of the isomer complex. On the other hand, the $[Eu(tta)_3(4\text{-picNO})_2]$ complex (Fig. S9b, red line) shows two strong emission peaks for the $^5D_0 \rightarrow {}^7F_0$ transition, indicating that two main Eu^{3+} symmetry sites are present, together with five peaks easily observed for the $^5D_0 \rightarrow {}^7F_1$ transition. This behavior may be assigned to the coexistence of residual water molecules in the Eu^{3+} coordination polyhedron derived from the hydrated complex, as small distortions may occur due to different Eu–O bond lengths [7,8].

Additionally, the emission intensity of $^5D_0 \rightarrow {}^7F_2$ transition is often used as a reference to support that Eu^{3+} ions occupy a non-centrosymmetric site. However, Eu^{3+} compounds with high polarizability ligands often present an intense hypersensitive transition, implying that the intensity ratio of $I(^5D_0 \rightarrow {}^7F_2)/I(^5D_0 \rightarrow {}^7F_1)$ cannot be

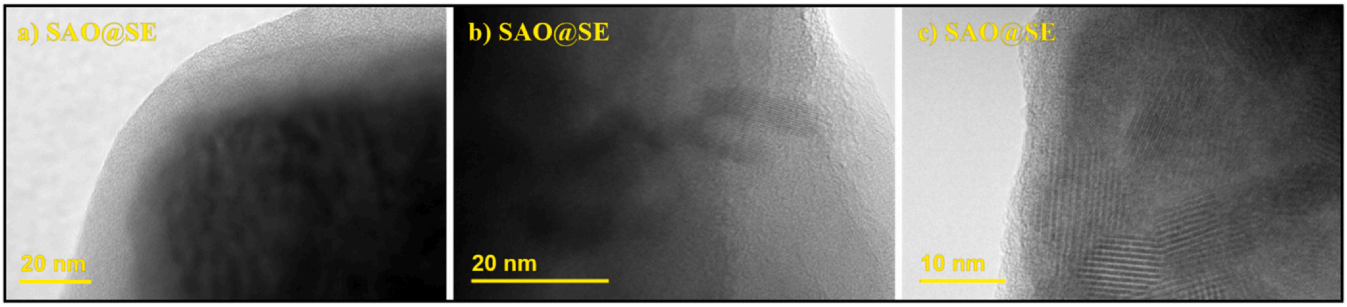

Fig. 4. TEM images of SAO@SE ($SrAl_2O_4$:Eu^{2+},Dy^{3+}@SiO_2-$[Eu(tta)_3(4\text{-picNO})_2]$) material acquired on different regions and magnifications (20 and 10 nm).

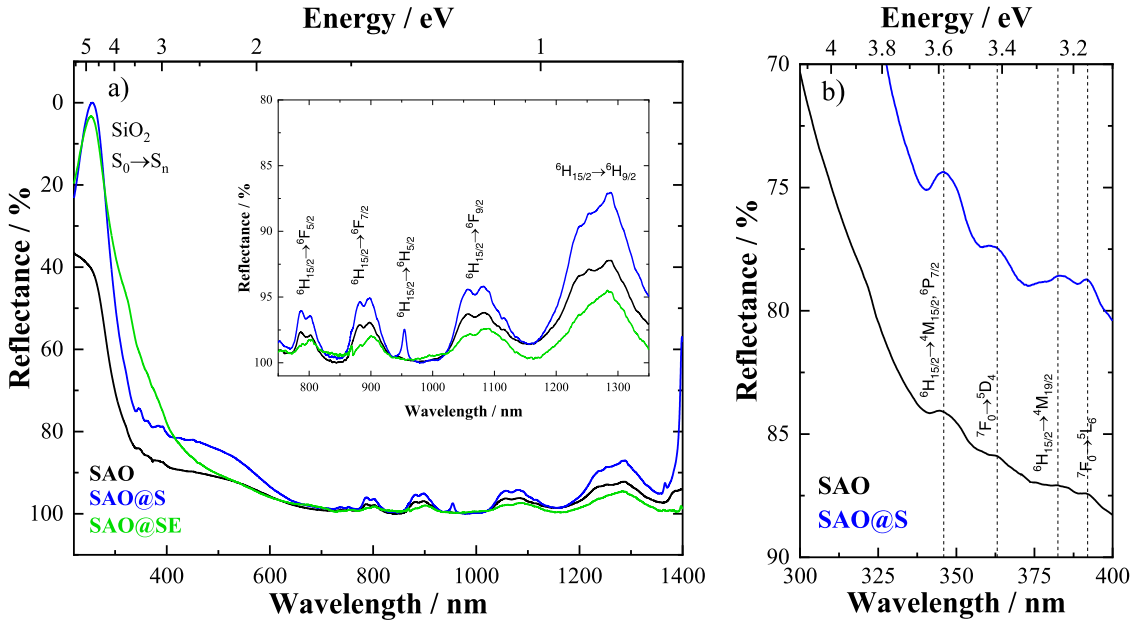

Fig. 5. DRS spectra of SAO, SAO@S and SAO@SE materials. (a) profiles display strong UV absorption alongside NIR Dy^{3+} intraconfigurational transitions (b) presents 4f–4f transitions observed in the near-UV region and.

the only symmetry parameter to be considered. Therefore, a more assertive approach is the correlation of both forced electric dipole (FED) transitions $^5D_0 \rightarrow {}^7F_J$ (J: 2, 4) with the magnetic dipole (MD) allowed transition $^5D_0 \rightarrow {}^7F_1$, where a centrosymmetric site is present if the MD transition presents higher intensity than both FED transitions. Thus, the analysis of the emission spectra implies that Eu^{3+} occupies non-centrosymmetric sites for the $[Eu(tta)_3(L)_2$ (L: H_2O or 4-picNO)] complexes.

Excitation spectra for the strontium aluminate compounds are presented in Fig. 6, where the spectral profiles display a strong dependence on the emission wavelength. For the SAO phosphor, excitation monitored on the Eu^{2+} emission (Fig. 6a, black line) shows a broad band of high-intensity absorption assigned to the (Eu^{2+}) $4f^7 \rightarrow 4f^65d^1$ transition coupled with the $^7F_{0-1} \rightarrow {}^5L_6$ transitions of non-reduced Eu^{3+} ion (transitions originated from the $^7F_1$ level of Eu^{3+} are indicated by an asterisk). When monitoring Eu^{3+} emission at 614 nm (Fig. 6a, red line), it is clearly seen the ligand-to-metal charge transfer (LMCT) band $[O^{2-} \rightarrow Eu^{3+}]$, [40] and intense (Eu^{3+}) 4f–4f absorption. Furthermore, when monitoring the 692 nm emission (Fig. 6a, blue line), the LMCT broad band practically disappears. Similarly, the SAO@S excitation spectra presented the predominant interconfigurational Eu^{2+} absorption (Fig. 6b, black line) and intense LMCT band along with the (Eu^{3+}) $^7F_0 \rightarrow {}^5L_6$ transition when monitored at the $^5D_0 \rightarrow {}^7F_2$ emission (Fig. 6b, red line). However, a considerable contribution of Eu^{2+} is also seen for the deep-red 692 nm emission band (Fig. 6b, blue line). In contrast, the SAO@SE sample displayed a

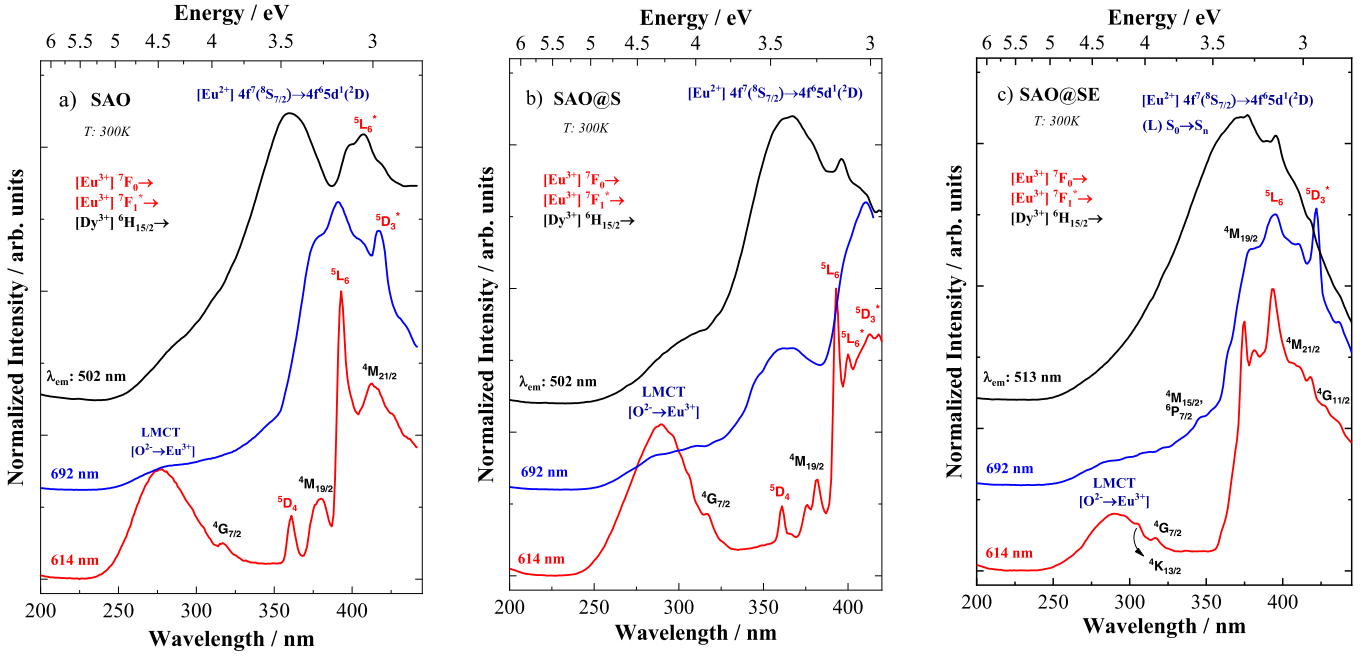

Fig. 6. Excitation spectra of (a) SAO, (b) SAO@S and (c) SAO@SE compounds monitored at 502–513 nm (Eu^{2+}, black lines), 614 nm (Eu^{3+}, red lines), and 692 nm (Cr^{3+}, blue lines) emissions.

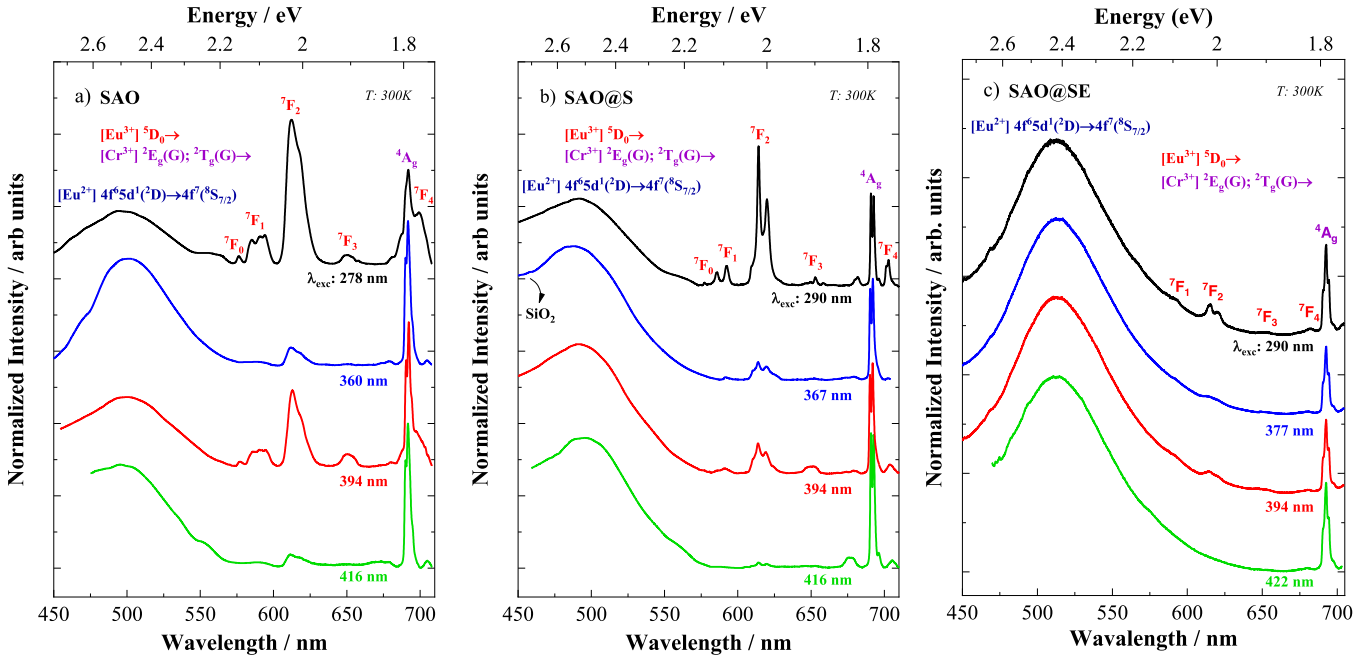

Fig. 7. Emission spectra of (a) SAO, (b) SAO@S and (c) SAO@SE compounds under excitation at 278–290 nm (Eu^{3+} - LMCT, black lines), 360–377 nm (Eu^{2+}- 4f-5d, blue lines), 394 and 416–422 nm (Eu^{3+} - 4f–4f, red and green lines).

broad absorption band (around 377 nm) assigned to a spectral overlap of (Eu^{2+}) $4f^7 \rightarrow 4f^6 5d^1$ and (L) $S_0 \rightarrow S_n$ transitions (Fig. 6**c**, black line). Besides, narrow absorption bands assigned to of Eu^{3+} and Dy^{3+} 4f–4f transitions are observed alongside the broad LMCT band when monitoring at 614 nm emission of Eu^{3+} (Fig. 6c, red line). When the excitation spectra of this material are monitored at 692 nm, it is clearly observed that the $^7F_0 \rightarrow {}^5L_6$ and $^7F_1 \rightarrow {}^5D_3$ transitions of Eu^{3+} ion are predominant (Fig. 6c, blue line).

Emission spectra of the synthesized strontium aluminate materials are exhibited in Fig. 7, where the SAO phosphor (Fig. 7a) presents a broad emission band at around 500 nm assigned to (Eu^{2+}) $4f^6 5d^1 \rightarrow 4f^7$ transition. Non-reduced Eu^{3+} ion is identified by the presence of the $^5D_0 \rightarrow {}^7F_{0-4}$ transitions, showing a high dependence of excitation energy for the hypersensitive $^5D_0 \rightarrow {}^7F_2$ transition. Remarkably, high sharp emission peaks were assigned to $^2E_g(G) \rightarrow {}^4A_g$ and $^2T_g(G) \rightarrow {}^4A_g$ transitions of Cr^{3+} ions as impurities embedded in the α-Al_2O_3 crystalline phase. This optical result give rise to characteristic R_1 (690 nm) and R_2 (692 nm) emission peaks of ruby gemstone, as previously reported by Monteiro et al. [34].

SAO@S similar emission profiles displayed a blue-shift due to SiO_2 phosphorescence overlapped with the Eu^{2+} broad emission band at different excitation energies (Fig. 7b). The high emission intensity of the $^5D_0 \rightarrow {}^7F_{0-4}$ transitions of the Eu^{3+} ion (black line) under LMCT excitation indicates efficient energy-transfer processes from the host matrix to the Eu^{3+} ion. For the SAO@SE material, the emission spectra (Fig. 7c) exhibit the highest emission intensity bands assigned to the (Eu^{2+}) $4f^6 5d^1 \rightarrow 4f^7$ transition centered around 513 nm (green color) at different excitation energies. In this sample, there is no contribution of the SiO_2 phosphorescence, and the (Eu^{3+}) $^5D_0 \rightarrow {}^7F_{0-4}$ transitions intensities diminished significantly. On the other hand, the emission peaks of Cr^{3+} ion still present a considerable intensity [8,27,41].

The experimental intensity parameters Ω_λ (λ: 2 and 4) of (Eu^{3+}) 4f–4f transitions [7,8,42] were determined for both the $[Eu(tta)_3(L)_2]$ (L: H_2O or 4-picNO) complexes, and Ω_2 intensity parameter was calculated for SAO compounds where the $^5D_0 \rightarrow {}^7F_{1-2}$ transitions were registered under 394 nm. The emission intensity is expressed by $I_{0\rightarrow J} = A_{0\rightarrow J} N_0$, where N_0 corresponds to the population of the emitting level ($^5D_0$), and $A_{0\rightarrow J}$ is defined as the spontaneous emission coefficient. For experimental determination of $A_{0\rightarrow J}$, it is possible to use the formally allowed MD transition ($^5D_0 \rightarrow {}^7F_1$) as a standard reference (practically one-hundred percent MD character). Thus, $A_{0\rightarrow J}$ values are obtained from Eq. (2).

$$A_{0\rightarrow J} = \left(\frac{S_{0\rightarrow J}}{S_{0\rightarrow 1}}\right) A_{0\rightarrow 1} \tag{2}$$

As the area under the curve (integrated intensity) is represented by $S_{0\rightarrow J}$ of the corresponding $^5D_0 \rightarrow {}^7F_J$ transitions. Hence Ω_λ (λ: 2, 4) presented in Table 1 were calculated from Eq. (3).

$$A_{0\rightarrow J} = \frac{4e^2\omega^3}{3hc^3}\frac{1}{2J+1}\chi \sum_{\lambda=2,4} \Omega_\lambda \langle {}^5D_0 \| U^{(\lambda)} \| {}^7F_J \rangle^2 \tag{3}$$

Where $\chi = n_0(n_0^2+2)^2/9$ is the Lorentz local field correction factor and n_0 is the material refractive index. The values of squared reduced matrix elements are listed in the literature as 0.0032 and 0.0023 for

Table 1
Experimental intensity parameters of A_{rad}; Ω_λ (λ: 2, 4) and $I(^5D_0 \rightarrow {}^7F_4)/I(^5D_0 \rightarrow {}^7F_2)$ determined from the emission spectra of $[Eu(tta)_3(L)_2]$ complexes (L: H_2O or 4-picNO) and SAO compounds under excitation at 394 nm.

Compounds	$\Omega_2(10^{-20}$ cm$^2)$	$\Omega_4(10^{-20}$ cm$^2)$	$I(^5D_0 \rightarrow {}^7F_4)/I(^5D_0 \rightarrow {}^7F_2)$	A_{rad}
$[Eu(tta)_3(H_2O)_2]$	26.3 ± 1.4	7.8 ± 0.2	0.3	955 ± 46
$[Eu(tta)_3(4\text{-picNO})_2]$	34.3 ± 2.3	8.4 ± 0.3	0.2	1202 ± 73
$SrAl_2O_4:Eu^{2+},Dy^{3+}$	6.9 ± 0.3	–	–	–
$SrAl_2O_4:Eu^{2+},Dy^{3+}@SiO_2$	12.1 ± 0.5	–	–	–

J: 2 and 4, respectively [7]. Furthermore, the total experimental spontaneous emission coefficient $A_{rad}(\sum A_{0\rightarrow J})$ for the $^5D_0$ emitting level and $I(^5D_0\rightarrow{}^7F_4)/I(^5D_0\rightarrow{}^7F_2)$ were also calculated for the europium complexes. The spectral baseline was corrected by interpolation, and emission intensity was normalized for all samples.

The high values of Ω_2 represent the intense characteristic luminescence of the $[Eu(tta)_3(L)_2]$ complexes (L: H_2O or 4-picNO). It is observed that after the coordination of the 4-picNO ancillary ligand, an increase in Ω_λ parameters (λ: 2 and 4) and A_{rad} is noted, confirming the increased emission intensity for the $^5D_0\rightarrow{}^7F_{2,4}$ transitions due to structural distortions. The intensity ratio of $I(^5D_0\rightarrow{}^7F_4)/I(^5D_0\rightarrow{}^7F_2)$ for $[Eu(tta)_3(L)_2]$ complexes diminish slightly in the 4-picNO complex, supporting an increase in emission intensity *via* $^5D_0\rightarrow{}^7F_2$ transition.

The Ω_2 parameters presented different values (7.3 and 12.4 × 10^{-20} cm^2) for the SAO and SAO@S compounds due to the distinct chemical environment of the Eu^{3+} ion in these materials [43]. The Ω_4 parameter was not evaluated for SAO compounds due to the strong spectral overlap of Eu^{3+} and Cr^{3+} emission bands around 695 nm. Furthermore, it is noted that intense broad band Eu^{2+} emission overlapping with the (Eu^{3+}) $^5D_0\rightarrow{}^7F_{1-2}$ transitions in SAO@SE phosphor restrained the evaluation of intensity parameters for this material.

The CIE (*Commission Internationale de l'éclairage*) diagram illustrating the color coordinates calculated from the emission spectra for all synthesized materials is shown in Fig. 8a. Also, Fig. 8b displays the luminescent behavior for all materials under 360 nm UV excitation. Through the positioning of each sample within the diagram, it is possible to identify a green emission on SAO (I) and SAO@SE (III) samples, where SiO_2 phosphorescence results in blue emission for the SAO@S (II) material. In contrast, both europium complexes (IV and V) present similar color coordinates, where intense red luminescence is seen through narrow Eu^{3+} 4–4f transitions.

VUV total photoluminescence excitation spectra (Fig. S10) showed intrinsic band gap absorption processes, and the first derivative of the total excitation profiles was used to estimate band gap energy, yielding values of E_g = 6.4, 6.9, and 6.6 ± 0.1 eV for SAO, SAO@S, and SAO@SE, respectively. These spectroscopic data are in good agreement with reported band gap values for $SrAl_2O_4$ [39], while the energies previously calculated *via* DRS for the functionalized SAO@S and SAO@SE materials do not directly correspond with the calculated energy gap (E_g) due to the contributions of the SiO_2 and organic ligands absorption bands.

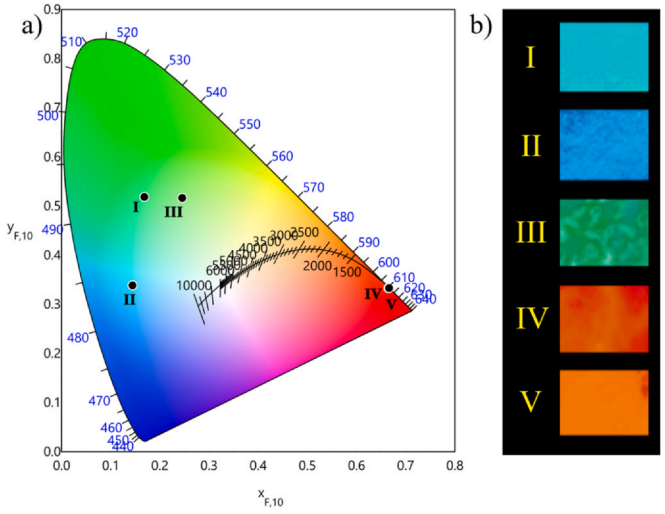

Fig. 8. (a) CIE diagram for I) SAO; II) SAO@S; III) SAO@SE; IV) $[Eu(tta)_3(H_2O)_2]$ and V) $[Eu(tta)_3(4\text{-picNO})_2]$. (b) Photographs of the synthesized materials were taken with a digital camera under UV (λ_{exc} = 366 nm) excitation.

3D emission spectra for the SAO phosphor in the VUV region (Fig. 9**a**) revealed a broad emission band originated from (Eu^{2+}) $4f^65d^1\rightarrow4f^7$ transition (centered around 523 nm) under excitation at near band gap energy. Moreover, the (Eu^{3+}) $^5D_0\rightarrow{}^7F_{1-4}$ (589, 614, 650 and 696 nm, respectively) and (Dy^{3+}) $^4F_{9/2}\rightarrow{}^6H_{13/2}$ (572 nm) transitions were also observed. In the 3D spectra of the SAO@S and SAO@SE materials (Fig. 9b,c), the Eu^{2+} emission band intensity decreases considerably, showing the (Dy^{3+}) $^4F_{9/2}\rightarrow{}^6H_{15/2},{}^6H_{13/2}$ (490 and 572 nm, respectively) and (Cr^{3+}) $^2E_g(G),{}^2T_g(G)\rightarrow{}^4A_g$ (692 nm) transitions as predominant. Furthermore, the band gap energy was determined by using the positioning of Eu^{2+} excited states near the bottom of the conduction band (CB) by the first derivative of the excitation spectra monitored at 523 nm, yielding E_g = 6.4, 6.7, and 6.7 eV for the SAO, SAO@S, and SAO@SE materials, respectively (Fig. S11). These optical features of the SAO, SAO@S, and SAO@SE materials are also presented on surface contour profiles in Fig. 9d-f.

Various energy levels associated with the tta and 4-picNO ligands and potential excitons (e^-–h^+ pairs) were also observed with values just below the lower edge of the CB (at around 6.4, 6.9, and 6.6 ± 0.1 eV), extending as far as 1 eV depth [44]. For the SAO phosphor (Fig. S12), excitation at high-energy states (5.4 and 6.1 eV) results in characteristic (Eu^{3+}) $^5D_0\rightarrow{}^7F_{1-4}$ luminescence, while the broad emission band of Eu^{2+} ion is only observed at E_g or higher energies.

In contrast, the functionalized materials SAO@S and SAO@SE (Fig. S13, S14) presented weak Eu^{2+} emission intensity at near band gap excitation, in favor of intense (Eu^{3+}) $^5D_0\rightarrow{}^7F_{1-4}$ transitions and (Cr^{3+}) $^2E_g(G),{}^2T_g(G)\rightarrow{}^4A_g$ transition within the exciton region [43], as well as a significant contribution of (Dy^{3+}) $^4F_{9/2}\rightarrow{}^6H_{15/2},{}^6H_{13/2}$ transitions were also detected. This optical behavior suggests that Eu^{2+} emission in both SAO@S and SAO@SE samples under VUV excitation in $SrAl_2O_4$ host matrix is not efficient.

The position of (Eu^{2+}) $4f^65d^1$ energy levels related to the top of the valence band (VB) of the $SrAl_2O_4$ matrix is expressed as the combination of the energies on the lower energy end for the first LMCT [$O^{2-}\rightarrow Eu^{3+}$] absorption band (3.8 eV) which corresponds to the position of (Eu^{2+}) $4f^7$ ground state related to the top of VB and the energy of the (Eu^{2+}) $4f^65d^1\rightarrow4f^7$ emission (2.48 eV, ~500 nm), where ΔE_{Eu2+} refers to the energy difference between the first excited and ground states of Eu^{2+} ion [27,45].

Thus, the lowest excited energy levels of Eu^{2+} are located near the CB edge (around 6.28 eV) in the $SrAl_2O_4$ matrix for the SAO phosphor. Minor changes in the positioning of these energy levels due to functionalization were observed, such as an E_g increase of about 0.3 eV and shifts of ± 0.1 eV and ± 0.05 eV for the LMCT absorption and Eu^{2+} emission, respectively. Hence, various defects near the CB edge may act as trapping centers for charge carriers (e^-), giving rise to the persistent luminescence observed for the prepared strontium aluminate compounds.

Furthermore, the SAO@SE functionalized compound presents relative energy values (ΔE_L) from overlapping of the (L) $S_0\rightarrow S_n$ transition and (Eu^{2+}) $4f^7\rightarrow4f^65d^1$ absorption transitions, suggesting potential energy transfer pathways involving the (L) S_n and (Eu^{2+}) $4f^65d^1$ excited states, promoting Eu^{2+} luminescence.

Finally, persistence luminescence decay curves of the SAO and SAO@SE materials are shown in Fig. 10 at maximum absorption band intensity (6.7 and 6.9 eV). The persistence luminescence decay time of the SAO@SE material greatly surpasses the signal recorded for the SAO phosphor, as the later rapidly decays to around 10% emission intensity which is maintained for close to 4 min after excitation. On the other hand, the functionalized SAO@SE compound have a much longer decay time until it reaches 10% emission intensity (about 140 s), and a more linear behavior can be observed despite some signal lifting events. Different defect contributions from trap concentrations, dopant (Eu^{3+}), co-dopant ions (Dy^{3+}) or vacancies ($V_O^{\bullet\bullet}$), functionalized silica and trap depth [20,23,46] must be taken into

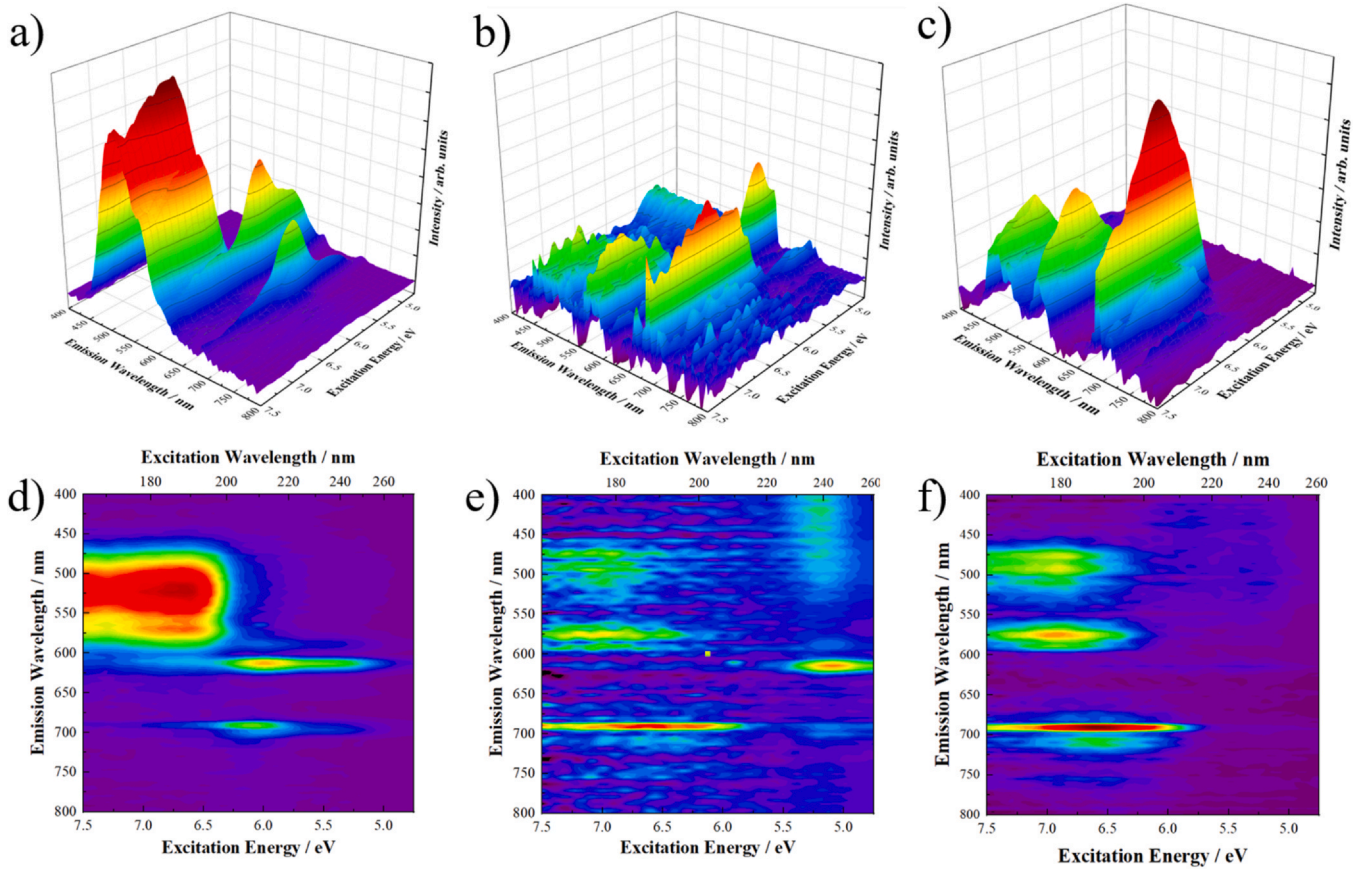

Fig. 9. 3D VUV emission spectra and surface contour profiles of (a,d) SAO, (b,e) SAO@S, and (c,f) SAO@SE.

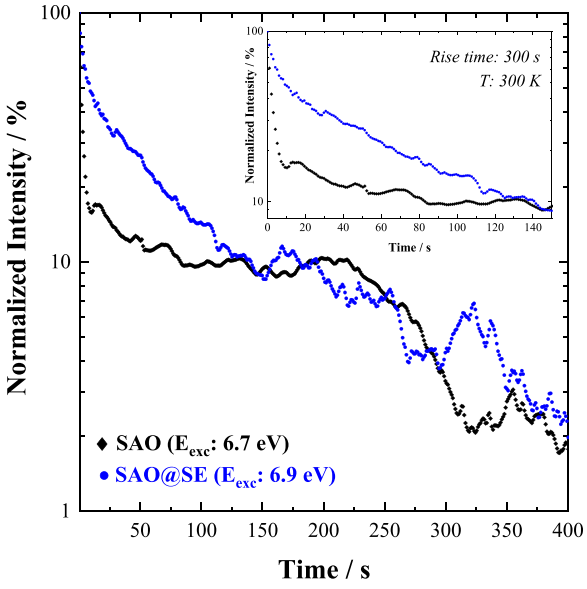

Fig. 10. Persistence decay curves of SAO ($SrAl_2O_4:Eu^{2+},Dy^{3+}$) and SAO@SE ($SrAl_2O_4:Eu^{2+},Dy^{3+}$@$SiO_2$-[$Eu(tta)_3(4\text{-picNO})_2$]) materials under near band gap excitation.

account for improving persistent luminescence decay time for the SAO@SE material.

Conventionally, the strontium aluminate persistent phosphor is prepared by ceramic methods, which favor defect formation and long persistence decay time that cannot be directly compared to phosphors prepared by wet-chemical routes. To obtain homogeneous and highly crystalline monoclinic $SrAl_2O_4$ defect formation is often minimized, directly affecting persistent luminescence. In fact, a fine tuning in defect concentration and high crystallinity in long persistent phosphors still poses a challenge, where the optimal balance for persistent luminescence may be difficult to achieve.

4. Conclusion

The preparation of the $SrAl_2O_4:Eu^{2+},Dy^{3+}$ phosphor was successfully carried out *via* the Pechini method and the further incorporation of a [$Eu(tta)_3(4\text{-picNO})_2$] complex supported by a SiO_2-R network through microwave-assisted synthesis was effective. FTIR data revealed the formation of a characteristic O–Si–O structure with terminal amino groups, while SEM images have shown surface alteration effects, imposing a porous-like framework on top of $SrAl_2O_4:Eu^{2+},Dy^{3+}$ particles. TEM images indicated crystalline phases in the SAO/SiO_2 interface. Elemental distribution maps presented homogeneous dopant dispersion, alongside the [$Eu(tta)_3(4\text{-picNO})_2$] distribution, tracked by the tta ligand (CF_3) group. PXRD analysis revealed a monoclinic structure for strontium aluminate, which undergoes several changes in functionalized compounds, and residual phase formation of $Sr_3Al_2O_6$ and α-Al_2O_3 by-products were also found. Spectroscopy investigation revealed intrinsic host matrix absorption and band gap energy was estimated to about 6.4 eV for the $SrAl_2O_4:Eu^{2+},Dy^{3}$ phosphor. Minor changes in band gap energy of the $SrAl_2O_4$ matrix on modified compounds were observed. Characteristic Eu^{2+} emission was predominant for all strontium aluminate compounds under UV excitation, and the SAO@SE compound presented the highest emission intensity. The presence of residual Eu^{3+} in the $SrAl_2O_4$ phase, as well as preferential

substitution of Cr^{3+} impurities in α-Al_2O_3 phase, were identified by their characteristic emission spectra. Experimental intensity parameters Ω_2 of the europium complexes and strontium aluminate materials presented different values, indicating distinct chemical environments around the Eu^{3+} ion for the modified materials. The electronic structure of the materials was also studied by VUV spectroscopy, and the SAO@SE material exhibited an increase in the persistence luminescence decay time compared to the SAO phosphor, where absorption and energy transfer processes from the Eu (tta) complex coupled with defect contribution may account for this optical behavior. This work demonstrates an approach of combining inorganic phosphors with rare-earth complexes as a pathway for enhancing emission intensity, outlining novel prospects for the development of rare-earth based persistent luminescent materials.

CRediT authorship contribution statement

Leonardo H. C. Francisco: Conceptualization, Methodology, Investigation, Writing - original draft. **Renan P. Moreira:** Investigation, Data Curation, Visualization. **Maria C. F. C. Felinto:** Conceptualization, Resources, Project administration, Writing - review & editing. **Veronica C. Teixeira:** Resources, Writing - review & editing. **Hermi F. Brito:** Supervision, Writing - review & editing. **Oscar L. Malta:** Formal analysis, Writing - review & editing.

Declaration of Competing Interest

The authors declare that they have no known competing financial interests or personal relationships that could have appeared to influence the work reported in this paper.

Acknowledgments

The authors thank the Brazilian Agencies: Sao Paulo Research Foundation (FAPESP), Coordination for the Improvement of Higher Education Personnel (CAPES), National Council for Scientific and Technological Development (CNPq), and National Nuclear Energy Commission (CNEN) for financial support, Dr. Douglas Galante, and Mr. Leonardo Kofukuda (TGM beamline staff) from the Brazilian Synchrotron Light Laboratory – Brazilian Center for Research in Energy and Materials (LNLS-CNPEM), Campinas, SP, Brazil, are gratefully acknowledged for their key assistance on vacuum ultraviolet spectroscopy experiments. Mr. Leonardo A. Diniz from the Chemical Systems Engineering Center, Department of Chemical Engineering, University of São Paulo, SP, Brazil, is thankfully acknowledged for cooperation on infrared spectroscopy measurements. Finally, we thank the support given by the Center for Lasers and Applications' Multiuser Facility at Nuclear and Energy Research Institute (IPEN-CNEN), São Paulo, SP, Brazil, for carrying out the SEM/EDS experiments.

Appendix A. Supporting information

Supplementary data associated with this article can be found in the online version at doi:10.1016/j.jallcom.2021.160608.

References

[1] J.-C.G. Bünzli, Lanthanide Luminescence: From a Mystery to Rationalization, Understanding, and Applications, in: J.-C.G. Bünzli, V.K. Pecharsky (Eds.), Handbook on the Physics and Chemistry of Rare Earths, 50 Elsevier, 2016, pp. 141–176, https://doi.org/10.1016/bs.hpcre.2016.08.003
[2] J.-C.G. Bünzli, Lanthanide photonics: shaping the nanoworld, Trends Chem. 1 (2019) 751–762, https://doi.org/10.1016/j.trechm.2019.05.012
[3] J.-C.G. Bünzli, A.-S. Chauvin, Lanthanides in Solar Energy Conversion, in: J.-C.G. Bünzli, V.K. Pecharsky (Eds.), Handbook on the Physics and Chemistry of Rare Earths, 44 Elsevier, 2014, pp. 169–281, https://doi.org/10.1016/B978-0-444-62711-7.00261-9
[4] Y. Li, M. Gecevicius, J. Qiu, Long persistent phosphors – from fundamentals to applications, Chem. Soc. Rev. 45 (2016) 2090–2136, https://doi.org/10.1039/C5CS00582E
[5] S.K. Singh, Red and near infrared persistent luminescence nano-probes for bioimaging and targeting applications, RSC Adv. 4 (2014) 58674–58698, https://doi.org/10.1039/C4RA08847F
[6] G. Chen, H. Ågren, T.Y. Ohulchanskyy, P.N. Prasad, Light upconverting core-shell nanostructures: nanophotonic control for emerging applications, Chem. Soc. Rev. 44 (2015) 1680–1713, https://doi.org/10.1039/C4CS00170B
[7] H.F. Brito, O.L. Malta, M.C.F.C. Felinto, E.E.S. Teotonio, Luminescence phenomena involving metal enolates, in: J. Zabicky (Ed.), The Chemistry of Metal Enolates, John Wiley & Sons, 2009, pp. 131–184, https://doi.org/10.1002/9780470682531.pat0419
[8] K. Binnemans, Interpretation of europium (III) spectra, Coord. Chem. Rev. 295 (2015) 1–45, https://doi.org/10.1016/j.ccr.2015.02.015
[9] J.-C.G. Bünzli, S.V. Eliseeva, Basics of Lanthanide Photophysics, in: P. Hänninen, H. Härmä (Eds.), Lanthanide Luminescence, Springer, Berlin, Heidelberg, 2011, pp. 1–45, https://doi.org/10.1007/4243_2010_3
[10] J.-C.G. Bünzli, On the design of highly luminescent lanthanide complexes, Coord. Chem. Rev (2015) 19–47, https://doi.org/10.1016/j.ccr.2014.10.013
[11] A.N.C. Neto, E.E.S. Teotônio, G.F. Sá, H.F. Brito, J. Legendziewicz, L.D. Carlos, M.C.F.C. Felinto, P. Gawryszewska, R.T. Moura, R.L. Longo, W.M. Faustino, O.L. Malta, Modeling intramolecular energy transfer in lanthanide chelates: A critical review and recent advances, in: J.-C. Bünzli, V. Pecharsky (Eds.), Handbook on the Physics and Chemistry of Rare Earths, 56 Elsevier, 2019, pp. 55–192, https://doi.org/10.1016/bs.hpcre.2019.08.001
[12] L.H.C. Francisco, M.C.F.C. Felinto, H.F. Brito, E.E.S. Teotonio, O.L. Malta, Development of highly luminescent PMMA films doped with Eu3+ β-diketonate coordinated on ancillary ligand, J. Mater. Sci. Mater. Electron. 30 (2019) 16922–16931, https://doi.org/10.1007/s10854-019-01639-9
[13] J. Feng, H. Zhang, Hybrid materials based on lanthanide organic complexes: a review, Chem. Soc. Rev. 42 (2013) 387–410, https://doi.org/10.1039/C2CS35069F
[14] F.P. Aguiar, I.F. Costa, J.G.P. Espínola, W.M. Faustino, J.L. Moura, H.F. Brito, T.B. Paolini, M.C.F.C. Felinto, E.E.S. Teotonio, Luminescent hybrid materials functionalized with lanthanide ethylenodiaminotetraacetate complexes containing β-diketonate as antenna ligands, J. Lumin. 170 (2016) 538–546, https://doi.org/10.1016/j.jlumin.2015.06.038
[15] L.U. Khan, D. Muraca, H.F. Brito, O.M. Londoño, M.C.F.C. Felinto, K.R. Pirota, E.E.S. Teotonio, O.L. Malta, Optical and magnetic nanocomposites containing Fe3O4@SiO2 grafted with Eu3+ and Tb3+ complexes, J. Alloys Compd. 686 (2016) 453–466, https://doi.org/10.1016/j.jallcom.2016.06.009
[16] H.F. Brito, J. Hölsa, T. Laamanen, M. Malkamäki, L.C.V. Rodrigues, Persistent luminescence mechanisms: human imagination at work, Opt. Mater. Express 2 (2012) 371–381, https://doi.org/10.1364/OME.2.000371
[17] K.V. Eeckhout, P.F. Smet, D. Poelman, Persistent luminescence in Eu2+-doped compounds: a review, Materials 3 (2010) 2536–2566, https://doi.org/10.3390/ma3042536
[18] P.F. Smet, K.V. Eeckhout, O.Q. De Clercq, D. Poelman, Persistent phosphors, in: J.-C.G. Bünzli, V.K. Pecharsky (Eds.), Handbook on the Physics and Chemistry of Rare Earths, 48 Elsevier, 2015, pp. 1–108, https://doi.org/10.1016/B978-0-444-63483-2.00001-6
[19] D. Dutczak, T. Jüstel, C. Ronda, A. Meijerink, Eu2+ luminescence in strontium aluminates, Phys. Chem. Chem. Phys. 17 (2015) 15236–15249, https://doi.org/10.1039/C5CP01095K
[20] E. Finley, A.M. Tehrani, J. Brgoch, Intrinsic defects drive persistent luminescence in monoclinic SrAl2O4:Eu2+, J. Phys. Chem. C 122 (2018) 16309–16314, https://doi.org/10.1021/acs.jpcc.8b04378
[21] T. Takeyama, T. Nakamura, N. Takahashi, M. Ohta, Electron paramagnetic resonance studies on the defects formed in the Dy(III)-doped SrAl2O4, Solid State Sci. 6 (2004) 345–348, https://doi.org/10.1016/j.solidstatesciences.2004.02.001
[22] P. Zeng, X. Wei, M. Yin, Y. Chen, Investigation of the long afterglow mechanism in SrAl2O4:Eu2+/Dy3+ by optically stimulated luminescence and thermoluminescence, J. Lumin. (2018) 400–406, https://doi.org/10.1016/j.jlumin.2018.03.088
[23] J.J. Joos, K. Korthout, L. Amidani, P. Glatzel, D. Poelman, P.F. Smet, Identification of Dy3+/Dy2+ as electron trap in persistent phosphors, Phys. Rev. Lett. 125 (2020) 033001–1–033001–33007, https://doi.org/10.1103/PhysRevLett.125.033001
[24] J. Botterman, J.J. Joos, P.F. Smet, Trapping and detrapping in SrAl2O4: Eu, Dy persistent phosphors: influence of excitation wavelength and temperature, 085147-1-085147-15, Phys. Rev. B 90 (2014) 085147, https://doi.org/10.1103/PhysRevB.90.085147
[25] V. Vitola, D. Millers, I. Bite, K. Smits, A. Supstaka, Recent progress in understanding the persistent luminescence in SrAl2O4: Eu, Dy, Mater. Sci. Technol. 35 (2019) 1661–1677, https://doi.org/10.1080/02670836.2019.1649802
[26] P. Dorenbos, Absolute location of lanthanide energy levels and the performance of phosphors, J. Lumin. 122–123 (2007) 315–317, https://doi.org/10.1016/j.jlumin.2006.01.155
[27] P. Dorenbos, Energy of the first 4f7→4f65d transition of Eu2+ in inorganic compounds, J. Lumin. 104 (2003) 239–260, https://doi.org/10.1016/S0022-2313(03)00078-4
[28] A.E. Danks, S.R. Hall, Z. Schneep, The evolution of 'sol–gel' chemistry as a technique for materials synthesis, Mater. Horiz. 3 (2016) 91–112, https://doi.org/10.1039/C5MH00260E
[29] I.P. Machado, V.C. Teixeira, C.C.S. Pedroso, H.F. Brito, L.C.V. Rodrigues, X-ray scintillator Gd2O2S:Tb3+ materials obtained by a rapid and cost-effective

microwave-assisted solid-state synthesis, J. Alloys Compd. 777 (2019) 638–645, https://doi.org/10.1016/j.jallcom.2018.10.348
[30] R.E.R. Hernandez, M.A. Rodriguez, J.F. Fernandez, Role of the oxidizing agent to complete the synthesis of strontium aluminate based phosphors by the combustion method, RSC Adv. 5 (2015) 3104–3112, https://doi.org/10.1039/C4RA10460A
[31] N.M. Bahadur, T. Furusawa, M. Sato, F. Kurayama, I.A. Siddiquey, N. Suzuki, Fast and facile synthesis of silica coated silver nanoparticles by microwave irradiation, J. Colloid Interface Sci. 355 (2011) 312–320, https://doi.org/10.1016/j.jcis.2010.12.016
[32] P.K. Shahi, A.K. Singh, S.K. Singh, S.B. Rai, B. Ullrich, Revelation of the technological versatility of the Eu(TTA)3Phen complex by demonstrating energy harvesting, ultraviolet light detection, temperature sensing, and laser applications, ACS Appl. Mater. Interfaces 7 (2015) 18231–18239, https://doi.org/10.1021/acsami.5b06350
[33] M. Avdeev, S. Yakovleva, A.A. Yaremchenkob, V.V. Kharton, Transitions between P21, P63(√3A), and P6322 modifications of SrAl2O4 by in situ high-temperature X-ray and neutron diffraction, J. Solid State Chem. 180 (2007) 3535–3544, https://doi.org/10.1016/j.jssc.2007.10.021
[34] M.A.F. Monteiro, H.F. Brito, M.C.F.C. Felinto, G.E.S. Brito, E.E.S. Teotonio, F.M. Vichi, R. Stefani, Photoluminescence behavior of Eu3+ ion doped into γ- and α-alumina systems prepared by combustion, ceramic and Pechini methods, Microporous Mesoporous Mat. 108 (2008) 237–246, https://doi.org/10.1016/j.micromeso.2007.03.045
[35] F.T.L. Muniz, M.A.R. Miranda, C.M. Santos, J.M. Sasaki, The Scherrer equation and the dynamical theory of X-ray diffraction, Acta Cryst. A72 (2016) 385–390, https://doi.org/10.1107/S205327331600365X
[36] V. Mishra, M.K. Warshi, A. Sati, A. Kumar, V. Mishra, A. Sagdeo, R. Kumar, P.R. Sagdeo, Diffuse reflectance spectroscopy: an effective tool to probe the defect states in wide band gap semiconducting materials, Mater. Sci. Semicond. Process. 86 (2018) 151–156, https://doi.org/10.1016/j.mssp.2018.06.025
[37] Kubelka-Munk Theory, in: H.R. Kang (Ed.), in: H.R. Kang (Ed.), Computational Color Technology, 16 SPIE Press, 2006, pp. 355–368 ISBN: 9780819481085.
[38] B.D. Viezbicke, S. Patel, B.E. Davis, D.P. Birnie, Evaluation of the Tauc method for optical absorption edge determination: ZnO thin films as a model system, Phys. Status Solidi B 252 (2015) 1700–1710, https://doi.org/10.1002/pssb.201552007
[39] J. Hölsä, T. Laamanen, M. Lastusaari, J. Niittykoski, P. Novák, Electronic structure of the SrAl2O4:Eu2+ persistent luminescence material, J. Rare Earths 27 (2009) 550–554, https://doi.org/10.1016/S1002-0721(08)60286-0
[40] L.C.V. Rodrigues, H.F. Brito, J. Hölsä, M. Lastusaari, Persistent luminescence behavior of materials doped with Eu2+ and Tb3+, Opt. Mater. Express 2 (2012) 382–390, https://doi.org/10.1364/OME.2.000382
[41] W.T. Carnall, G.L. Goodman, K. Rajnak, R.S. Rana, A systematic analysis of the spectra of the lanthanides doped into single crystal LaF3, J. Chem. Phys. 90 (1989) 3443–3457, https://doi.org/10.1063/1.455853
[42] C. Larry, Complexes, in: Karl A. Gschneidner, Jr., Le.Roy Eyring (Eds.), Handbook on the Physics and Chemistry of Rare Earths, 3 Thompson, 1979, pp. 209–297, https://doi.org/10.1016/S0168-1273(79)03008-7
[43] R.A. Sá Ferreira, S.S. Nobre, C.M. Granadeiro, H.I.S. Nogueira, L.D. Carlos, O.L. Malta, A theoretical interpretation of the abnormal 5D0→7F4 intensity based on the Eu3+ local coordination in the Na9[EuW10O36]·14H2O polyoxometalate, J. Lumin. 121 (2006) 561–567, https://doi.org/10.1016/j.jlumin.2005.12.044
[44] M. Fox, Optical Properties of Solids, 2 ed., Oxford University Press, New York, 2010 ISBN: 9780199573363.
[45] P. Dorenbos, Systematic behaviour in trivalent lanthanide charge transfer energies, J. Phys. Condens. Matter 15 (2003) 8417–8434, https://doi.org/10.1088/0953-8984/15/49/018
[46] P. Dorenbos, Mechanism of persistent luminescence in Eu2+ and Dy3+ codoped aluminate and silicate compounds, J. Electrochem. Soc. 152 (2005) H107–H110, https://doi.org/10.1149/1.1926652